LEARNABLE DOUGLAS-RACHFORD ITERATION AND ITS APPLICATIONS IN DOT IMAGING

Jiulong Liu*

Department of Mathematics, National University of Singapore, Singapore 119076

Nanguang Chen

Department of Biomedical Engineering, National University of Singapore, Singapore 117583

Hui Ji

Department of Mathematics, National University of Singapore, Singapore 119076

(Communicated by Martin Burger)

Abstract. How to overcome the ill-posed nature of inverse problems is a pervasive problem in medical imaging. Most existing solutions are based on regularization techniques. This paper proposed a deep neural network (DNN) based image reconstruction method, the so-called DR-Net, that leverages the interpretability of existing regularization methods and adaptive modeling capacity of DNN. Motivated by a Douglas-Rachford fixed-point iteration for solving ℓ_1-norm relating regularization model, the proposed DR-Net learns the prior of the solution via a U-Net based network, as well as other important regularization parameters. The DR-Net is applied to solve image reconstruction problem in diffusion optical tomography (DOT), a non-invasive imaging technique with many applications in medical imaging. The experiments on both simulated and experimental data showed that the proposed DNN based image reconstruction method significantly outperforms existing regularization methods.

1. **Introduction.** Image reconstruction in medical imaging is about generating high-quality images, i.e., visual representation of internal structures of physiological organs, from measurements collected by the instrument. It can be formulated as solving a linear inverse problem:

$$y = Au + \epsilon, \tag{1}$$

where y denotes collected measurements, u denotes the image, and ϵ denotes measurement noise, and the operator A models image acquisition process. Different imaging techniques have different forms of the measurement matrix A. As the matrix A is usually ill-posed in medical imaging, the problem (1) requires solving a challenging linear inverse problem. Moreover, the trend of medical imaging collecting less measurement using the instrument with weaker radiation power. For instance, computed tomography (CT) imaging prefers to lower radiation dose to reduce the object exposure to X-ray radiation, and magnetic resonance imaging (MRI) prefers to use low k-space data sampling rate to reduce scan time. Diffusion optical tomography (DOT) is an emerging technique to image hemodynamic changes in

human breast for its non-invasive nature, low cost, and portability. As a result, in these techniques, the signal-to-noise ratio (SNR) of measurement y is lower, and the matrix A is more ill-posed.

The ill-posedness of a linear inverse problem usually can be resolved by imposing certain prior on the image u when solving (1), which can be done by formulating it as an optimization problem:

$$(2) \qquad \frac{1}{2}\|Au - y\|_2^2 + \lambda p(u).$$

where $p(\cdot)$ is the regularization term derived from the image prior. In the past, many predefined image priors have been proposed for solving inverse problems in imaging. To list some, squares of ℓ_2-norm based Tikhonov regularization that assumes the smoothness of image [29], total variation (TV) [27] and wavelet transform [4] based ℓ_1-norm relating regularization that exploit the sparsity prior of image gradients, and non-local regularization that assumes the recurrence prior of local image patches [7, 20, 18, 5]. These regularization techniques see their applications in many medical image reconstruction tasks, including DOT imaging (see e.g. [6, 15]). As these predefined image priors are not adaptive to the variations among different images, the reconstruction quality from these regularization methods often is not satisfactory, especially when collected measurements are few and of low SNR. For instance, many image details are erased when using Tikhonov regularization, and there are stair-casing artifacts shown in the reconstructed images using ℓ_1-norm relating regularization methods.

In recent years, as a powerful machine learning tool, deep learning also sees its applications in medical image reconstruction. Instead of using DNN as a black box to directly model the mapping between the measurements and the image, a more promising approach is to include the knowledge of imaging physics in the deep learning based method. Earlier works [13, 33, 14] used DNN as a post-process denoising to refine the results reconstructed from some existing methods. Recently, a more appealing approach is integrating DNN into the reconstruction process. One popular approach is to unroll some iterative algorithms of a regularization method and replace the operation involving image prior by a DNN based learnable operation. Such a learned image prior is then adaptive to target images and it is expected to perform better than those using predefined image priors. There has been an enduring effort on developing such optimization unrolling based DNN for medical image reconstruction. For example, proximal gradient descent based methods [2, 1, 23] for CT reconstruction, and ADMM-Net[28], learned variational network [12] for MRI reconstruction.

The basic procedure to design a DNN that unrolls an optimization method with learnable prior is given as follows. Taking ℓ_1-norm based regularization methods for example, these methods formulate the reconstruction problem as solving the following optimization problem:

$$(3) \qquad \|Au - y\|_2^2 + \lambda\|\mathcal{D}u\|_1,$$

where the operator $\mathcal{D}$ can be a differential operator or wavelet transform. The alternating direction method of multipliers (ADMM) method [3, 9] is one representative

algorithm for solving (3), which reads

$$(4) \quad \begin{cases} u^{k+1} = \arg\min_{u} \|Au - y\|^2 + \frac{\varrho}{2}\|\mathcal{D}u - d^k + b^k\|_2^2; \\ d^{k+1} = \arg\min_{d} \lambda\|d\|_1 + \frac{\varrho}{2}\|\mathcal{D}u^{k+1} - d + b^k\|_2^2; \\ b^{k+1} = b^k + (\mathcal{D}u^{k+1} - d^{k+1}). \end{cases}$$

An image reconstruction algorithm with learned prior is about replacing the second step in the iteration above by an NN based function $\Phi(\cdot; \vartheta)$ with trainable weights ϑ. The function Φ maps $\mathcal{D}u^{k+1}$ to d^k and b^k. It can be seen that the image prior induced by the regularization term $p(\cdot)$ is replaced by a more powerful one learned from training data.

In this paper, we propose a new unrolling scheme for medical image reconstruction, which includes both the inversion with learnable parameters and the prior learned by a NN. The proposed deep learning based image reconstruction method, called DR-Net, is then applied to the challenging image reconstruction problem in DOT imaging. The proposed DR-Net is motivated from a fixed-point iteration based reformulation of (4), i.e., the so-called Douglas-Rachford iteration. There are several concatenated stages in the DR-Net. Each stage corresponds to one step of the iteration. Each stage contains two blocks: (i) inversion block and (ii) de-artifacting block. The inversion block reconstructs the image from the collected measurement, assisted by additional information from the de-artifacting block in the previous stage. In our approach, such additional information is the image de-artifacted in the previous stage under a learned linear transform $\mathcal{D}$. The de-artifacting block is for refining the image reconstructed in the inversion block using image prior learned from a NN. The DR-Net is built using the blocks that have clear physics meaning. The experiments in image reconstruction for DOT imaging showed that the DR-Net does not suffer from of over-fitting on both our simulated dataset and experimental dataset, and it noticeably outperformed representative regularization methods.

The rest of this paper is organized as follows. In section 2, we give a brief introduction to medical image reconstruction and then propose a learnable Douglas-Rachford iteration via convolutional neural networks(CNN). Section 3 gives a brief introduction to DOT imaging and applies the DR-Net to solve image reconstruction problem in DOT imaging. The performance of the DR-Net for DOT image reconstruction is evaluated and analyzed in Section 4. Section 5 concludes the paper.

2. **Learnable Douglas-Rachford iteration for image reconstruction.** Regularization has been one main tool for solving inverse problems which are typically ill-conditioned. The performance of these methods remains unsatisfactory when being used for reconstructing images when measurements are few and of low SNR. Motivated by impressive performance of deep learning based methods for many image processing problems(see e.g. [31, 16]), as well as image reconstruction in CT and MRI (see e.g. [28, 1, 21]), this section aims at developing a new DNN-based image reconstruction method that can be used in many medical imaging techniques.

With the concatenation of many simple nonlinear operations parameterized by millions of adjustable weights, DNN can model very complex functions. To utilize prior knowledge of imaging physics, one approach is to unroll the iterative scheme of existing regularization methods and replace the predefined prior based module by a deep learning based module. For example, several deep learning based methods have been proposed for MRI image reconstruction that unrolls different numerical methods for solving ℓ_1-norm relating regularization models. The ADMM-net

method [28] unrolls the ADMM method and replaces the thresholding operation by an NN-based function. The method proposed in [1] unrolls the primal-dual method, and the method [21] unrolls the variable splitting methods.

In this section, we propose a method for medical image reconstruction, which unrolls a re-formulated version of the ADMM algorithm from the perspective of Douglas-Rachford iteration, a fixed-point iteration. Recall that the ADMM for solving (3) is a three-block iterative scheme given as follows.

$$(5) \quad \begin{cases} u^{k+1} = \Psi(d^k - b^k, y) := \arg\min_u \|Au - y\|^2 + \frac{\rho}{2}\|\mathcal{D}u - (d^k - b^k)\|_2^2, \\ d^{k+1} = \Phi(\mathcal{D}u^{k+1} + b^k) := \arg\min_d \|d\|_1 + \frac{\rho}{2}\|\mathcal{D}u^{k+1} - d + b^k\|_2^2, \\ b^{k+1} = b^k + (\mathcal{D}u^{k+1} - d^{k+1}). \end{cases}$$

Following the procedure described in [8], we can reformulate the iteration scheme (5) as a fixed-point iteration. Define the variable

$$(6) \quad t^{k+1} = b^k + \mathcal{D}u^{k+1}.$$

Then, we have $d^{k+1} = \Phi(t^{k+1})$, and thus

$$b^{k+1} = b^k + (\mathcal{D}u^{k+1} - d^{k+1}) = t^{k+1} - d^{k+1} = t^{k+1} - \Phi(t^{k+1}).$$

Plug them into the first equation in (5), we have then

$$(7) \quad t^{k+1} = b^k + \mathcal{D}u^{k+1} = b^k + \mathcal{D}(\Psi(y, d^k - b^k)) = t^k - \Phi(t^k) + \mathcal{D}(\Psi(2\Phi(t^k) - t^k, y))).$$

The fixed-point iteration (7) is also called Douglas-Rachford iteration [17]. In our method, we propose to implement the inversion mapping Ψ with learnable parameters ρ and NN-based learnable transform $\mathcal{D}$, and to replace the prior-based mapping Φ by NN-based learnable function. Let $\mathcal{D}_\theta$ and Φ_ϑ denote the functions modeled by the NN with parameters θ and ϑ. Then the learnable version of the Douglas-Rachford iteration (7) can be expressed as

$$(8) \quad t^{k+1} = T_{\Theta_k}(t^k) = t^k - \Phi_{\vartheta_k}(t^k) + \mathcal{D}_{\theta_k}\Psi(2\Phi_{\vartheta_k}(t^k) - t^k, y, \rho_k, \mathcal{D}_{\theta_k})$$

for $k = 1, 2, \cdots, N$, where the NN parameters are

$$\Theta = \{\Theta_k\}_{k=1}^N = \{\rho_k, \theta_k, \vartheta_k\}_{k=1}^N$$

The optimization problem in the first step of the iteration (5) is quadratic, and thus we have an analytic solution:

$$(9) \quad \Psi(v, y, \rho, \mathcal{D}_\theta) = (A^\top A + \rho\mathcal{D}_\theta^\top \mathcal{D}_\theta)^{-1}(A^\top y + \rho\mathcal{D}_\theta^\top v).$$

The linear system above usually is large-scale in medical imaging. Thus, we need to call some iterative solver for computational efficiency, e.g., conjugate gradient method. In our approach, not only the parameter ρ in (9) is a learnable parameter, but also the linear operator $\mathcal{D}_\theta$ is a function with learnable parameters θ. For computational feasibility, the operator $\mathcal{D}_\theta$ needs to fit well a computational architecture of NN. Thus, we propose to adopt the operator $\mathcal{D}$ in the form of a filter bank:

$$(10) \quad \mathcal{D} : u \to \theta * u = [\theta_\ell * u]_{\ell=1}^L,$$

where $*$ denotes the 2D discrete convolution operator here. The operator $\mathcal{D}$ defined by (10) can be implemented via a CNN in which the bias is set to 0, and the activation function is set to identity. For completeness, the backward derivative of the inversion block with a one-layer and one-channel CNN used in backpropagation is listed below.

Proposition 1. *Consider a function* $f : \mathbb{R}^n \to \mathbb{R}$. *Let* $\mathcal{D}_\theta$ *denote the transform defined by* (10) *and* Ψ *the function defined by* (9). *The backward derivatives of* $f(\Psi(v, y, \rho, \mathcal{D}_\theta))$ *are given by*

(11)

$$
\begin{cases}
\dfrac{\partial f(\Psi(v, y, \rho, \mathcal{D}_\theta))}{\partial v} = \rho \mathcal{D}_\theta \left(A^\top A + \rho \mathcal{D}_\theta^\top \mathcal{D}_\theta \right)^{-1} \dfrac{\partial f}{\partial \Psi} \\[2mm]
\dfrac{\partial f(\Psi(v, y, \rho, \mathcal{D}_\theta))}{\partial y} = A \left(A^\top A + \rho \mathcal{D}_\theta^\top \mathcal{D}_\theta \right)^{-1} \dfrac{\partial f}{\partial \Psi} \\[2mm]
\dfrac{\partial f(\Psi(v, y, \rho, \mathcal{D}_\theta))}{\partial \rho} = (\mathcal{D}_\theta^\top v - \Psi)^\top \left(A^\top A + \rho \mathcal{D}_\theta^\top \mathcal{D}_\theta \right)^{-1} \dfrac{\partial f}{\partial \Psi} \\[2mm]
\dfrac{\partial f(\Psi(v, y, \rho, \mathcal{D}_\theta))}{\partial \theta} = \Psi[-\cdot, -\cdot] * \mathcal{D}_\theta \left(A^\top A + \rho \mathcal{D}_\theta^\top \mathcal{D}_\theta \right)^{-1} \dfrac{\partial f}{\partial \Psi} \\[2mm]
\qquad\qquad + \left((v - \mathcal{D}_\theta \Psi) * (\mathcal{D}_\theta \left(A^\top A + \rho \mathcal{D}_\theta^\top \mathcal{D}_\theta \right)^{-1} \dfrac{\partial f}{\partial \Psi}) \right)[-\cdot, -\cdot].
\end{cases}
$$

where $[-\cdot, -\cdot]$ *reverses the order of the elements along two axes.*

Proof. See Appendix A for the detailed derivation. $\square$

The backward derivatives for the case of 3D images with 3D convolution can be similarly obtained. The linear systems involved in the calculation of backward derivatives defined in (32) can be solved by the conjugate gradient method.

Using a learnable function modeled by NN to replace the mapping Φ derived from the predefined prior has been proposed to solve many general image restoration problems, including image denoising [30, 22, 31], super-resolution and many others [10, 25, 11]. In the proposed approach, we also adopt a CNN-based function to model the function Φ in (5) in the de-artifacting block by

$$ d := \Phi_\vartheta(t), $$

which is learned over training samples.

3. DR-Net for DOT image reconstruction.

3.1. Introduction to image reconstruction in DOT.
In non-invasive diffusive optical imaging, both light sources and detectors are outside of the human body. As near-infrared light from light sources is strongly scattered in soft tissue, the photons do not form straight-line beams anymore. Indeed, they become diffusive and probe a rather broad volumetric region after propagating through the body, which is measured and recorded in detectors. The so-called *image reconstruction* problem is then about how to translate the measurement collected in detectors into a map, the so-called *optical image*, that relates to optical properties of tissues. Photon propagation in a turbid media can be described by a diffusion equation parameterized by the absorption and scattering coefficients, and photon density is the function to be solved. The goal of image reconstruction is to estimate the optical properties including absorption and diffusion coefficients within the tissue from collected measurements. There are many applications of DOT in medical imaging, e.g. optical mammography. Optical mammography uses DOT to image hemodynamic changes in the human breast. Owing to its non-invasive nature and low cost, optical mammography allows more frequent scans of patients than X-ray mammography does, and its portability makes it a good complementary device for pre-screening. Also,

FIGURE 1. A prototype time-resolved diffuse optical tomography system designed for optical imaging of human breast [24]

the DOT image contains additional functional information for differentiating malignant cancers from benign lesions. There are different experimental approaches to DOT. The majority of existing DOT systems can be classified into two categories: *continuous wave* (CW) and *frequency domain* (FD). In a CW system, the output of light sources is roughly constant, and the intensity of time-independent photon density waves is measured. In an FD system, light sources are modulated at a frequency in the typical range of 50 - 200 MHz so that phase delay of photon density wave can be obtained besides amplitude. As time-resolved measurement of diffusive light contains more information for facilitating image reconstruction process, recent DOT technology can capture time-resolved measurement of diffusive light with faster data acquisition and high signal to noise ratio; see Fig 1 for an illustration of a time-solved DOT system designed for early detection of breast cancers.

During image acquisition in optical mammography, a human subject lays prone on the top of the machine so that her breasts are suspended into the imaging chamber, in which two transparent plates compress the breasts gently to ensure good contact with the skin. A laser head emits a collimated beam that illuminates the breast tissue perpendicularly through one of the compression plates, while three detectors on the opposite side collect the diffusive light transmitted through the tissue. A large number of measurements can be made by simultaneously raster scanning the sources and the detectors.

Time-resolved optical measurements can be predicted by a time-dependent diffusion equation that describes the propagation of diffusive light in turbid medium:

$$(12) \qquad \kappa \nabla^2 \phi(\mathbf{r}, t) - \mu_a \phi(\mathbf{r}, t) = -\frac{1}{c} \frac{\partial \phi(\mathbf{r}, t)}{\partial t} - S(\mathbf{r}, t),$$

where $\phi(\mathbf{r}, t)$ is the measurable fluence rate (or photon density) at time t and position $\mathbf{r}$, $S(\mathbf{r}, t)$ is the optical source going into the medium, c is the light velocity in the tissue, and

$$(13) \qquad \kappa = \frac{1}{3 \left[\mu_a + (1 - g)\mu_s \right]} = \frac{1}{3\mu_{st}} = \frac{l_r}{3}$$

is the photon diffusion coefficient. In (13), μ_a denotes absorption coefficient, μ_s denotes scattering coefficient, g denotes isotropic factor, $\mu_{st} = (1 - g)\mu_s + \mu_a$ denotes linear transport coefficient, and $l_{tr} = \frac{1}{\mu_{st}}$ denotes transport mean free path. Given incident source intensity, their corresponding locations, the measurements and their detector locations, how to reconstruct the optical properties, including both absorption and scattering coefficients, from diffusion equation (12) is a non-linear and ill-posed inverse problem. If the distributions of optical properties in a volume are given, the diffusion equation (12) can then be solved by some numerical methods, such as finite element method (FEM). Then, we have a forward problem expressed as

$$(14) \qquad\qquad\qquad Y = \mathbf{F}(\mu)$$

where the optical property μ contains both absorption coefficient μ_a and scattering coefficient μ_s (or diffusion coefficient κ), and Y is the collected measurement. In practice, we use the optical property μ representing total distribution, e.g., a tumor in the homogeneous background which has initial optical properties estimation μ_0, and usually the total optical property μ is close to its initial optical property estimation μ_0. The increased optical property $\delta\mu$ will consequently result in a change in the measurement. Thus, instead of reconstructing μ, we construct the perturbation of $\delta\mu$

$$(15) \qquad \delta\mu = \begin{pmatrix} \delta\mu_a \\ \delta\mu_s \end{pmatrix} = \begin{pmatrix} \mu_a \\ \mu_s \end{pmatrix} - \begin{pmatrix} \mu_{0a} \\ \mu_{0s} \end{pmatrix} := \begin{pmatrix} u_a \\ u_s \end{pmatrix} := u.$$

By taking the first-order Taylor approximation to the measurement Y, we have then

$$(16) \qquad\qquad \delta Y = \frac{\partial \mathbf{F}}{\partial \mu}\delta\mu + o(||\delta\mu||_2) := y.$$

In the end, image reconstruction problem using time-resolved optical measurements can be simplified as the problem of solving the following linear system

$$(17) \qquad\qquad\qquad y = Au$$

where $y = \delta Y$, A is the Jacobian matrix w.r.t. the first-order derivative of $\frac{\partial \mathbf{F}}{\partial \mu}$, and $u = \delta\mu$. In general, the Jacobian matrix A is non-invertible, and thus a certain prior needs to be imposed on the solution u when solving (17).

The so-called regularization method reformulates the ill-posed linear inverse problem (17) as a general optimization problem (3). One often-used regularization method for medical imaging, including the DOT reconstruction, is Tikhonov regularization [6]

$$p(u) = \|\nabla u\|_2^2,$$

where ∇ denotes the first-order spatial differential operator. It can be seen that Tikhonov regularization assumes that the desired solution is smooth with its energy concentrated in low frequencies. Thus, the corresponding result tends to be overly smoothed as the high frequencies of the result that contains edge information is either erased or severely attenuated. To keep sharp edges in the reconstructed image, a better approach is using ℓ_1-norm relating regularization, e.g., TV-based regularization, which considers

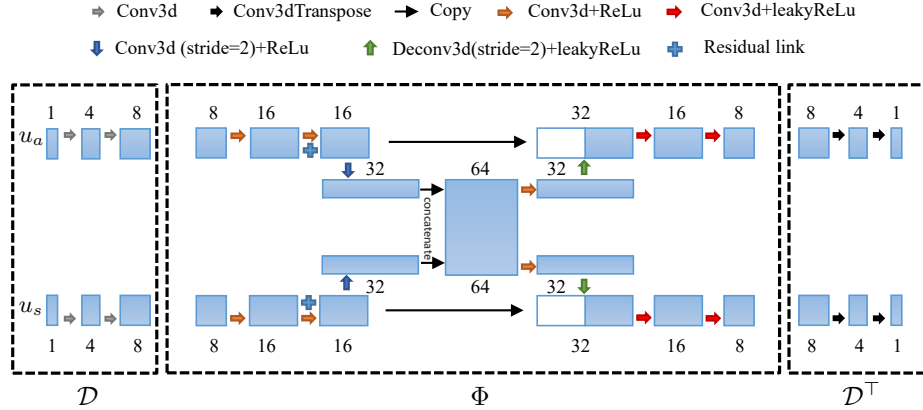$$(18) \qquad\qquad\qquad p(u) = \|\nabla u\|_1$$

FIGURE 2. X-Net: architecture of components of DR-Net, including $\mathcal{D}_\theta$, Φ_ϑ and $\mathcal{D}_\theta^\top$. Note that the weights of $\mathcal{D}_\theta$ and $\mathcal{D}_\theta^\top$ can be shared with each other, or learned individually.

in the optimization model. TV-based regularization not only sees its wide usages in image reconstruction problems in CT and MRI, but also is used for image reconstruction in DOT, e.g. [15]. Nevertheless, the details recovered from TV regularization is still not very satisfactory, and there are often noticeable stair-casing artifacts in the result. For meeting the needs in practice, there is certainly the need to develop a more powerful reconstruction algorithm with higher resolution for DOT.

3.2. **DR-Net for image reconstruction in DOT imaging.** Image reconstruction on DOT imaging is about reconstructing both absorption coefficients u_a and scattering coefficients u_s from collected measurements y. Based on the learnable Douglas-Rachford iteration (8), we develop the so-called DR-Net for image reconstruction in DOT imaging. In the proposed DR-Net, there are two NNs. One is for the transform $\mathcal{D}_\theta$ in inversion block which is implemented using one-layer standard CNN without bias and nonlinear activation. The other is for the mapping Φ_ϑ in the de-artifacting block. The architecture of Φ_ϑ is based on the so-called U-Net [26]. Instead of using a plain version of U-Net, we made some modifications to fit the need of our problem. More specifically, let the variable u^{k+1} representing the estimation of the image at the $(k+1)$-th stage. The image contains two entities: u_a^{k+1} representing absorption coefficients, and u_s^{k+1} representing scattering coefficients. Although these two entities have rather different distributions on intensity, they are correlated to each other to a certain degree. Thus, these two entities are updated via two U-Nets, but the intermediate output of each entity is copied to the NN of the other one. We call such a NN as X-Net. Such similar architectures can also be found in [32, 19] to explore the structural similarity. See Fig 2 for the architecture of one stage of the proposed DR-Net for medical image reconstruction.

Consider L training samples:

$$\{(\boldsymbol{y}_\ell, \tilde{\boldsymbol{u}}_\ell)\}_{\ell=1}^L,$$

where $\boldsymbol{y}_\ell$ denotes the measurement and $\tilde{\boldsymbol{u}}_\ell$ denotes the corresponding truth image. For each input measurement y, let $u_N := \mathcal{D}_{\theta_N}^\top t^N$ denotes the output of the NN.

The loss function for training is then defined as

$$(19) \qquad L(\Theta) = \frac{1}{2}\sum_{\ell=1}^{L} \|\boldsymbol{u}_{\ell,N} - \tilde{\boldsymbol{u}}_{\ell}\|_2^2 + R(\Theta),$$

where Θ denote the set of the weights of the whole DNN that include the weights of all inversion blocks $\{\rho_k, \vartheta_k\}_{k=1}^{N}$ and de-artifacting blocks $\{\theta_k\}_{k=1}^{N}$, and the regularization $R(\Theta)$ for the Θ is considered as following

$$(20) \qquad R(\Theta) = \sum_{k=1}^{N-1}\sum_{\ell=1}^{L} \alpha_k \|\boldsymbol{u}_{\ell,k} - \tilde{\boldsymbol{u}}_{\ell}\|_2^2,$$

with the parameters α can be empirically set as $\alpha_k = \frac{1}{N-k+2}$. The weights of NN are then learned by minimizing the loss function (19). Once we have a good estimation on the weights Θ^*, for any input measurement y, the image can be constructed by the forwarding pass of y in the DNN (8) with the weights Θ.

4. **Experimental evaluation.** In this section, the proposed DR-Net for DOT image reconstruction is evaluated on both simulated data and experimental datasets collected from the time-resolved DOT system illustrated in Fig 1. Our code and data are available at https://github.com/jiulongliu/SOFPI-DR-Net-DOT.

Through the experiments, the DNN is set up as follows. Totally $N = 6$ stages are used in the proposed method, and the learned ρ in the inversion block $[\rho_k]_{k=1}^{6} = [5.9731, 5.2703, 4.1330, 3.0843, 2.5850, 2.0939]$. The NN is trained using Adam method with the following training parameters: learning rate 0.001, number of epoch 300 and batch size 128. The weights of $\mathcal{D}_\theta$ and $\mathcal{D}_\theta^{\top}$ are not shared with each other for this DOT reconstruction as we found that it can speed up the training for this experiment.

4.1. **Dataset and experimental set-up.** The acquisition of experimental data is done on a time-solved diffuse optical tomography system shown in Figure 1. A liquid tissue phantom, mostly composed of a homogeneous 0.6% intralipid solution, was used to mimic the optical properties of normal breast tissue. A small target was fabricated by mixing epoxy resin, TiO_2, and Ink to achieve a reduced scattering coefficient similar to that of the intralipid solution and a higher absorption coefficient around $0.5\,\mathrm{cm}^{-1}$. The target size was 10 mm in length and 8 mm in diameter. During phantom imaging experiments, the target was suspended in the Intralipid solution with various depths to simulate a small solid tumor surrounded by normal breast tissues. We acquired several times of fluence for the same target position and the times of experiment are listed in Table 1 in which $I_i(i = 1, \cdots)$ denote the measured fluence. The raw dataset (Table 1) is used to generate 348 measurements for training and 31 measurements for testing by
(21)

$$Y(i,j,s) = \log\left(\frac{1/(\#Q)\sum\limits_{q\in Q}\sum\limits_{t} I_q(i,j,t)e^{p(s)t}}{\sum\limits_{t} I_0(i,j,t)e^{p(s)t}}\right), 1 \le i \le 13, 1 \le j \le 12, 1 \le s \le 27.$$

where p denotes Laplace parameter, the measured fluence of multiple times are averaged, and I_0 denotes the measured fluence without presenting the phantom, and Q is a subset of the measurements obtained at the same position by multiple

experiments. Note that the testing dataset is obtained by presenting the phantom in different positions from the training dataset.

TABLE 1. Experimental dataset $(Q \neq \phi)$

Depth(mm)	5	15	25	35	45
raw dataset	$T_1 = \{I_i\}_1^5$	$T_2 = \{I_i\}_6^{13}$	$T_3 = \{I_i\}_{14}^{18}$	$T_4 = \{I_i\}_{15}^{19}$	$T_5 = \{I_i\}_{20}^{24}$
Augmentation	$Q \subset T_1$	$Q \subset T_2$	$Q \subset T_3$	$Q \subset T_4$	$Q \subset T_5$
Data size	31	255	31	31	31
Purpose	Training	Training	Testing	Training	Training

The augmented experimental dataset is not sufficient for training the model (8) with good generalization. Instead, it is observed that the model (8) can have much better generalization performance when it is trained with an additional dataset simulated by the following procedure. The simulated dataset is generated as follows. We first set up phantom in 4 kinds of shapes, which are denoted as S, composed of cubic containers of size 5mm × 5mm × 5mm (1 voxel), shown in Fig 3. Then, the different materials with different optical properties are placed in the containers. In the simulation, let $\mathcal{U}$ denote uniform distribution and $\mathcal{N}$ denote normal distribution. Then, the phantom (ground truth) $\tilde{u} = [\tilde{u}_a, \tilde{u}_s]^\top$ is set as

$$\tilde{u}_a(i,j,k) = \begin{cases} \sim \mathcal{U}(0.4, 0.6), & \text{if} \quad (i,j,k) \in S; \\ 0, & \text{otherwise,} \end{cases}$$

and

$$\tilde{u}_s(i,j,k) = \begin{cases} \sim \mathcal{U}(0.2, 0.3), & \text{if} \quad (i,j,k) \in S; \\ 0, & \text{otherwise.} \end{cases}$$

for $1 \leq i \leq 13, 1 \leq j \leq 12, 1 \leq k \leq 9$. The measurements are synthesized by

$$(22) \qquad\qquad y = A(\tilde{u} + \eta) = A(\begin{bmatrix} \tilde{u}_a + 0.2\eta_a \\ \tilde{u}_s + 0.1\eta_s \end{bmatrix}),$$

where the noise η_a of each pixel and the noise η_s of each pixel independently and identically follow normal distribution $\mathcal{N}(0, 0.05)$. The training samples are then generated by sliding the shape S over different pixels and randomly draw values in (22) for 3 times. Totally

$$(13 \times 12 \times 9 + 12 \times 12 \times 9 + 13 \times 11 \times 9 + 12 \times 11 \times 9) \times 3 = 15525$$

samples are generated as the training set for training the NN. The testing data is simulated by sliding the shape S to position $(5, 7, k), 1 \leq k \leq 9$ and randomly draw values in (22) for once, which leads to a testing dataset of 36 instances. It is noted that the intensity of all instances in the training dataset and that of the testing dataset is randomly drawn from the normal distribution, and thus they are not correlated.

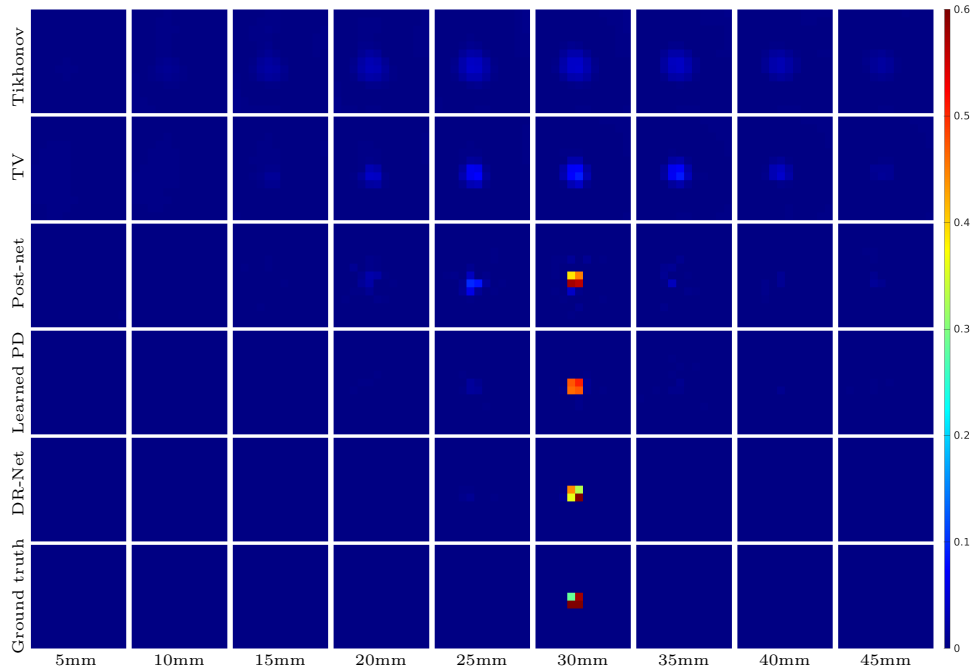FIGURE 3. Phantom shapes for simulated data, each cubic container is of size $5mm \times 5mm \times 5mm$ ($1 \times 1 \times 1$ voxel).

FIGURE 4. Reconstructed absorption coefficients from simulated measurements with phantom size of $10mm \times 10mm \times 5mm$ in depth of $30mm$.

4.2. **The results.** In comparison to the proposed method, totally four methods are included for reconstructing images from both simulated data and experimental data. Two are non-learning-based regularization methods including Tikhonov regularization method and the TV-based regularization method. Two are deep learning based methods. One is called Post-net, which learns NN-based denoiser for post-processing image reconstructed from the TV regularization method [13, 33, 14], and the other is called learnable primal dual, which is an NN-based learnable primal dual method [1] (named as Learned PD). The NNs used in these two methods are both based on the same NN used in the proposed method for modeling the mapping Φ.

For simulated data, the results from different methods are visualized in Figure 5 for image slices of absorption coefficients and Figure 5 for image slices of scattering coefficients. For experimental data, the results from different methods are visualized in Figure 6 for image slices of absorption coefficients and Figure 7 for image slices of scattering coefficients. It can be seen that the results from the proposed DR-Net for DOT image reconstruction are of better resolution than that from the other four compared methods.

The quantitative evaluation of the reconstructed image quality in terms of contrast is based on the contrast-to-noise ratio (CNR) defined by

$$(23) \qquad \mathrm{CNR}(G, B) = \frac{M_G - M_B}{\sqrt{\sigma_G^2 + \sigma_B^2}}$$

where M_G, M_B are the mean intensities of the target and the background respectively, and σ_G, σ_B are standard deviations of the target and the background respectively. Here we evaluate each pixel which locates in the phantom (G) with its
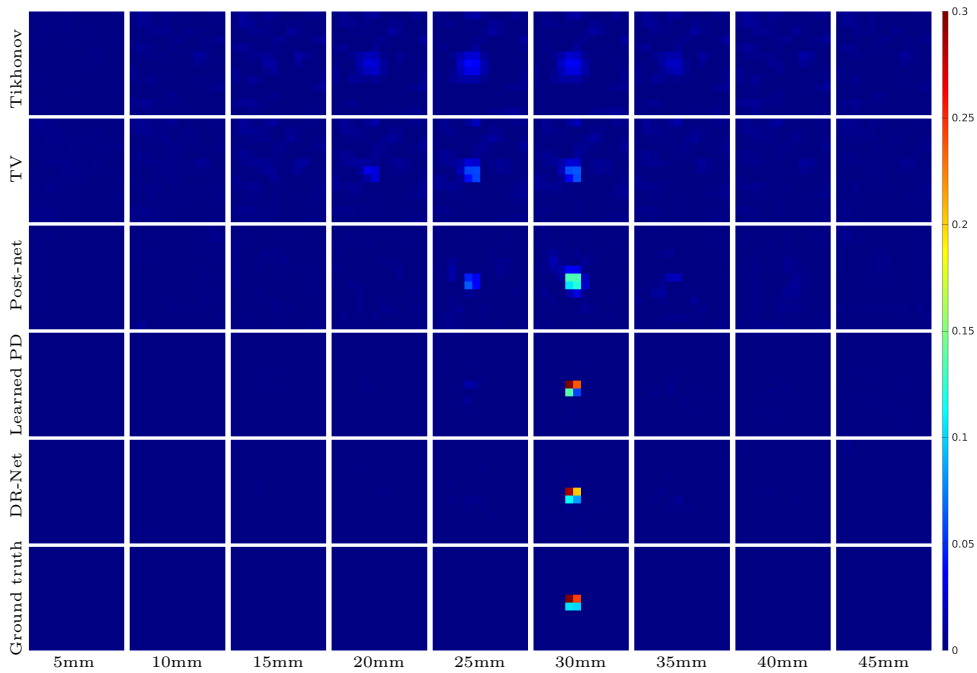
FIGURE 5. Reconstructed scattering coefficients from simulated measurements with phantom of $10mm \times 10mm \times 5mm$ in depth of $30mm$.

TABLE 2. CNR of reconstructed phantom in Fig. 4-7 from simulated data and experimental data

Data	Results	Pixel	Tikhonov	TV	Post-net	Learned PD	DR-Net
sim	u_a	1	1.04	1.33	13.53	83.65	**125.94**
		2	1.46	1.28	11.27	77.82	**158.06**
		3	1.58	1.42	16.02	66.74	**100.64**
		4	1.94	2.17	15.58	75.16	**218.52**
	u_s	1	1.48	2.33	6.06	84.81	**187.18**
		2	1.94	2.32	5.61	77.82	**123.83**
		3	1.18	1.17	4.83	**66.74**	51.55
		4	1.36	2.51	5.61	**75.16**	34.63
exp	u_a	1	1.75	1.12	3.14	0.92	**5.09**
		2	2.21	2.39	1.70	4.93	**15.57**
	u_s	1	1.38	0.64	1.16	0.96	**7.09**
		2	2.40	1.55	2.21	6.7607	**18.98**

neighborhood and background pixels with radius of 1 pixel (B). The quantitative evaluation on the reconstructed image quality in terms of reconstruction accuracy is based on PSNR and SSIM. See Table 2 & 3 for quantitative comparison of the images reconstructed from both simulated and experimental test data using five methods. It can be seen that the proposed DR-Net method noticeably outperformed the other two non-learning regularization methods and two learning-based methods.
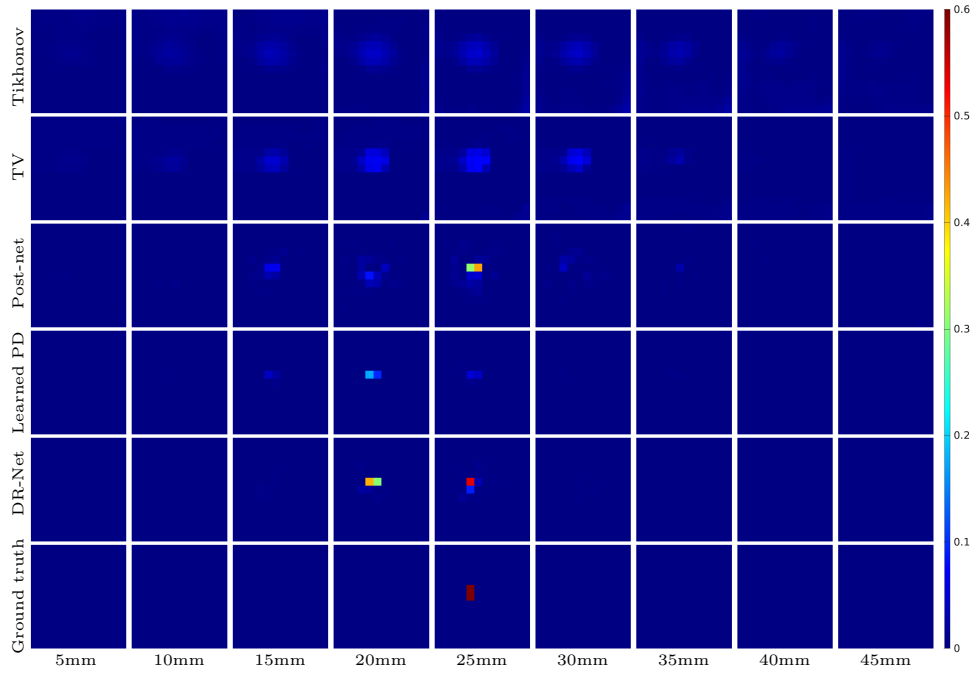
FIGURE 6. Reconstructed absorption coefficients from experimental measurements $\{I_{15}, I_{16}, I_{17}\}$ with phantom of $5mm \times 10mm \times 5mm$ in depth of $25mm$.

TABLE 3.   Averaged PSNR and SSIM of reconstructed images from simulated data and experimental data

Data	Results	Measure	Tikhonov	TV	Post-net	Learned PD	DR-Net
sim	u_a	PSNR	31.68	31.91	38.22	39.46	**40.98**
		SSIM	0.9182	0.9275	0.9759	0.9807	**0.9881**
	u_s	PSNR	31.29	32.04	34.56	**41.34**	38.03
		SSIM	0.9301	0.9401	0.9740	**0.9914**	0.9898
exp	u_a	PSNR	28.16	28.36	29.01	28.07	**29.33**
		SSIM	0.8612	0.8871	0.9441	0.9412	**0.9460**
	u_s	PSNR	28.92	29.20	29.94	29.46	**31.13**
		SSIM	0.8870	0.9239	0.9587	0.9700	**0.9779**

To show that the learned $\mathcal{D}_{\theta^*}$ is beneficial for alleviating ill-posedness of the inversion procedure and the learned Φ_{ϑ^*} can de-artifact gradually, we also plot the intermediate absorption coefficients $\{u_a^k, \mathcal{D}_{\theta_k^*}^\top v_a^k\}_{k=1}^6$ of (8) in Fig. 8 & 9 .

5. **Conclusion.** In this paper, we developed a DNN based method for image reconstruction in DOT, which is motivated by unrolling a fixed-point reformulation of the ADMM method, one prevalent numerical solver for ℓ_1-norm relating regularization models. By leveraging physics-driven regularization methods and powerful modeling capability of deep learning, the proposed method can lead to great performance gain over existing regularization methods. The evaluation of both simulated datasets and experimental datasets showed that the proposed method significantly improved the resolution and accuracy of the reconstructed images in DOT.
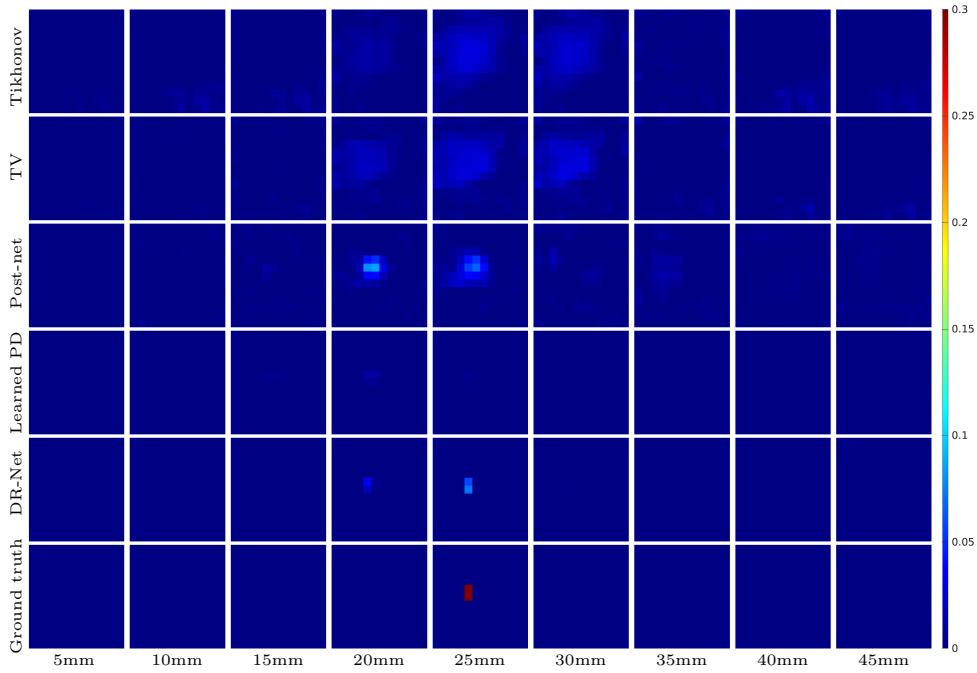
FIGURE 7. Reconstructed scattering coefficients from experimental measurements $\{I_{15}, I_{16}, I_{17}\}$ with phantom of $5mm \times 10mm \times 5mm$ in depth of $25mm$.

Appendix A. **Proof for proposition 1.**

Proposition 1. *Let $f : \mathbb{R}^n \to \mathbb{R}$ and $\mathcal{D}_\theta u = \theta * u$, and the backward derivatives of $f(\Psi(v, y, \rho, \mathcal{D}_\theta))$ (9) with respect to v, y, ρ and θ from the derivatives of $f(\Psi(v, y, \rho, \mathcal{D}_\theta))$ with respect to Ψ can be correspondingly given by*
(24)
$$
\begin{cases}
\dfrac{\partial f(\Psi(v, y, \rho, \mathcal{D}_\theta))}{\partial v} = \rho \mathcal{D}_\theta \left(A^\top A + \rho \mathcal{D}_\theta^\top \mathcal{D}_\theta\right)^{-1} \dfrac{\partial f}{\partial \Psi} \\[2ex]
\dfrac{\partial f(\Psi(v, y, \rho, \mathcal{D}_\theta))}{\partial y} = A \left(A^\top A + \rho \mathcal{D}_\theta^\top \mathcal{D}_\theta\right)^{-1} \dfrac{\partial f}{\partial \Psi} \\[2ex]
\dfrac{\partial f(\Psi(v, y, \rho, \mathcal{D}_\theta))}{\partial \rho} = (\mathcal{D}_\theta^\top v - \Psi)^\top \left(A^\top A + \rho \mathcal{D}_\theta^\top \mathcal{D}_\theta\right)^{-1} \dfrac{\partial f}{\partial \Psi} \\[2ex]
\dfrac{\partial f(\Psi(v, y, \rho, \mathcal{D}_\theta))}{\partial \theta} = \Psi[-\cdot, -\cdot] * \mathcal{D}_\theta \left(A^\top A + \rho \mathcal{D}_\theta^\top \mathcal{D}_\theta\right)^{-1} \dfrac{\partial f}{\partial \Psi} \\[2ex]
\qquad\qquad + ((v - \mathcal{D}_\theta \Psi) * (\mathcal{D}_\theta \left(A^\top A + \rho \mathcal{D}_\theta^\top \mathcal{D}_\theta\right)^{-1} \dfrac{\partial f}{\partial \Psi}))[-\cdot, -\cdot].
\end{cases}
$$

Proof. Since $\mathcal{D}_\theta u = \theta * u$, its adjoint operator with respect to u,

(25)
$$
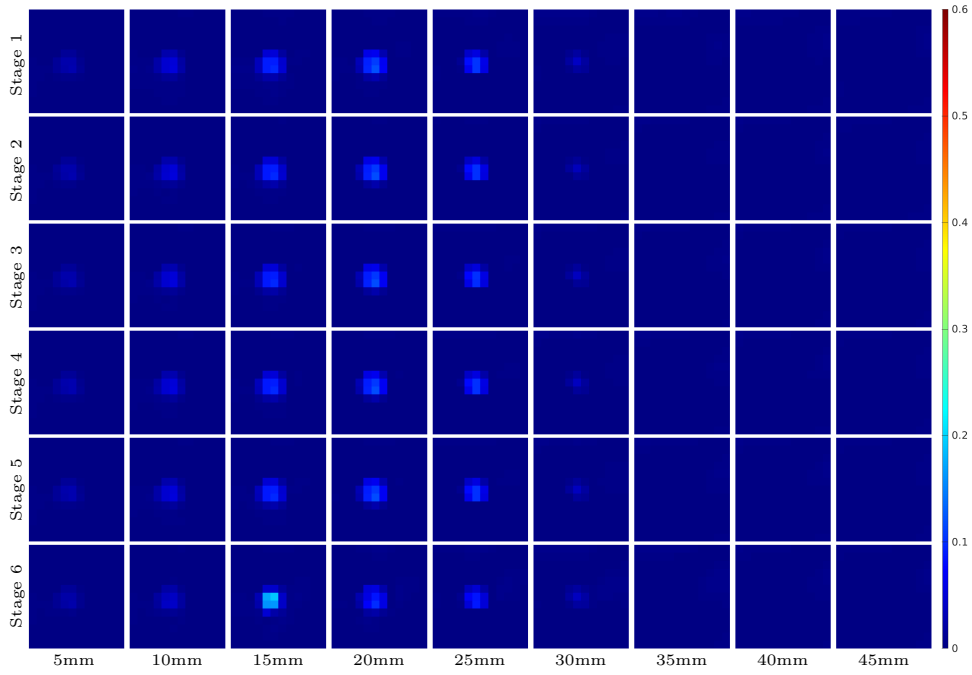\mathcal{D}_\theta^\top v = \theta[-\cdot, -\cdot] * v
$$

FIGURE 8. Outputs of inversion blocks for absorption coefficients u_a^k of all stages in inference phase from simulated measurements with phantom size of $10mm \times 10mm \times 5mm$ in depth of $15mm$.

where $-\cdot$ represents flipping the variable around its axis which follows the fact

$$\langle \theta * u, v \rangle = \langle \tilde{\theta} \odot \tilde{u}, \tilde{v} \rangle = \langle \tilde{u}, \bar{\tilde{\theta}} \odot \tilde{v} \rangle = \langle u, \theta[-\cdot, -\cdot] * v \rangle \tag{26}$$

where $\tilde{\cdot}$ denotes the Fourier Transform and $\bar{\cdot}$ denotes the conjugate. Therefore, we obtained

$$\partial \mathcal{D}_\theta u = \partial \theta * u + \theta * \partial u = \partial \theta * u + \mathcal{D}_\theta \partial u \tag{27}$$

and

$$\partial \mathcal{D}_\theta^\top v = \partial \theta[-\cdot, -\cdot] * v + \theta[-\cdot, -\cdot] * \partial v = \partial \theta[-\cdot, -\cdot] * v + \mathcal{D}_\theta^\top \partial v. \tag{28}$$

and

$$\begin{aligned}
\partial \mathcal{D}_\theta^\top \mathcal{D} u &= \partial[\theta[-\cdot, -\cdot] * (\theta * u)] \\
&= \partial \theta[-\cdot, -\cdot] * (\theta * u) + \theta[-\cdot, -\cdot] * (\partial \theta * u) + \theta[-\cdot, -\cdot] * (\theta * \partial u) \\
&= \partial \theta[-\cdot, -\cdot] * (\mathcal{D}_\theta u) + \mathcal{D}_\theta^\top (\partial \theta * u) + \mathcal{D}_\theta^\top \mathcal{D}_\theta u
\end{aligned} \tag{29}$$

Then (9) can be differentiated with respect to v, y, ρ and the filter θ, i.e.

$$\begin{aligned}
\left(A^\top A + \rho \mathcal{D}_\theta^\top \mathcal{D}_\theta\right) \partial \Psi + \Psi \partial \rho + \rho[\partial \theta[-\cdot, -\cdot] * (\mathcal{D}_\theta \Psi) + \mathcal{D}_\theta^\top (\partial \theta * \Psi)] \\
= A^\top \partial y + \mathcal{D}_\theta^\top v \partial \rho + \rho[\partial \theta[-\cdot, -\cdot] * v + \mathcal{D}_\theta^\top \partial v]
\end{aligned} \tag{30}$$

and then

$$\begin{aligned}
\partial \Psi = \left(A^\top A + \rho \mathcal{D}_\theta^\top \mathcal{D}_\theta\right)^{-1} [\rho \mathcal{D}_\theta^\top \partial v + A^\top \partial y + (\mathcal{D}_\theta^\top v - \Psi) \partial \rho \\
+ \rho(\partial \theta[-\cdot, -\cdot] * (v - \mathcal{D}_\theta \Psi) - \mathcal{D}_\theta^\top (\partial \theta * \Psi))].
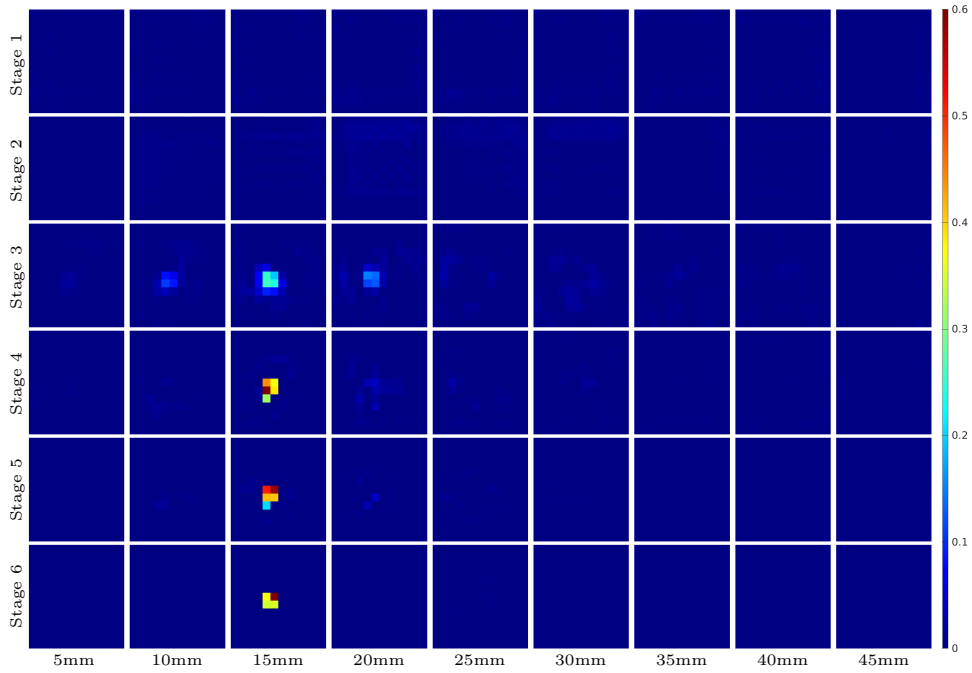\end{aligned} \tag{31}$$

FIGURE 9. Outputs of de-artifacting blocks for absorption coefficients $\mathcal{D}_{\theta_k^*}^{\top} v_a^k$ of all stages in inference phase from simulated measurements with phantom size of $10mm \times 10mm \times 5mm$ in depth of $15mm$.

The backward derivatives of $f(\Psi(v, y, \rho, \mathcal{D}_\theta))$ with respect to v , y , ρ and θ from the derivatives of $f(\Psi(v, y, \rho, \mathcal{D}_\theta))$ with respect to Ψ can be correspondingly given by

(32)
$$
\begin{cases}
\dfrac{\partial f(\Psi(v, y, \rho, \mathcal{D}_\theta))}{\partial v} = \rho \mathcal{D}_\theta \left(A^\top A + \rho \mathcal{D}_\theta^\top \mathcal{D}_\theta \right)^{-1} \dfrac{\partial f}{\partial \Psi} \\[2ex]
\dfrac{\partial f(\Psi(v, y, \rho, \mathcal{D}_\theta))}{\partial y} = A \left(A^\top A + \rho \mathcal{D}_\theta^\top \mathcal{D}_\theta \right)^{-1} \dfrac{\partial f}{\partial \Psi} \\[2ex]
\dfrac{\partial f(\Psi(v, y, \rho, \mathcal{D}_\theta))}{\partial \rho} = (\mathcal{D}_\theta^\top v - \Psi)^\top \left(A^\top A + \rho \mathcal{D}_\theta^\top \mathcal{D}_\theta \right)^{-1} \dfrac{\partial f}{\partial \Psi} \\[2ex]
\dfrac{\partial f(\Psi(v, y, \rho, \mathcal{D}_\theta))}{\partial \theta} = \Psi[-\cdot, -\cdot] * \mathcal{D}_\theta \left(A^\top A + \rho \mathcal{D}_\theta^\top \mathcal{D}_\theta \right)^{-1} \dfrac{\partial f}{\partial \Psi} \\[2ex]
\qquad\qquad + ((v - \mathcal{D}_\theta \Psi) * (\mathcal{D}_\theta \left(A^\top A + \rho \mathcal{D}_\theta^\top \mathcal{D}_\theta \right)^{-1} \dfrac{\partial f}{\partial \Psi}))[-\cdot, -\cdot].
\end{cases}
$$

$\square$

REFERENCES

[1] J. Adler and O. Öktem, Learned primal-dual reconstruction, *IEEE Transactions on Medical Imaging*, **37** (2018), 1322–1332.

[2] J. Adler and O. Öktem, Solving ill-posed inverse problems using iterative deep neural networks, *Inverse Problems*, **33** (2017), 124007, 24 pp.

[3] S. Boyd, N. Parikh, E. Chu, B. Peleato and J. Eckstein, Distributed optimization and statistical learning via the alternating direction method of multipliers, *Foundations and Trends® in Machine Learning*, **3** (2011), 1–122.

[4] J.-F. Cai, B. Dong, S. Osher and Z. Shen, Image restoration: Total variation, wavelet frames, and beyond, *J. Amer. Math. Soc.*, **25** (2012), 1033–1089.

[5] J.-F. Cai, H. Ji, Z. Shen and G.-B. Ye, Data-driven tight frame construction and image denoising, *Appl. Comput. Harmon. Anal.*, **37** (2014), 89–105.

[6] N. Cao, A. Nehorai and M. Jacob, Image reconstruction for diffuse optical tomography using sparsity regularization and expectation-maximization algorithm, *Optics Express*, **15** (2007), 13695–13708.

[7] K. Dabov, A. Foi, V. Katkovnik and K. Egiazarian, Image denoising with block-matching and 3d filtering, in *Image Processing: Algorithms and Systems, Neural Networks, and Machine Learning*, 6064, Proc. SPIE, 2006, 606414.

[8] D. Davis and W. Yin, A three-operator splitting scheme and its optimization applications, *Set-Valued Var. Anal.*, **25** (2017), 829–858.

[9] T. Goldstein and S. Osher, The split Bregman method for $L1$-regularized problems, *SIAM J. Imaging Sci.*, **2** (2009), 323–343.

[10] I. Goodfellow, J. Pouget-Abadie, M. Mirza, B. Xu, D. Warde-Farley, S. Ozair, et al., Generative adversarial nets, in *Advances in Neural Information Processing Systems*, 2014, 2672–2680.

[11] I. Gulrajani, F. Ahmed, M. Arjovsky, V. Dumoulin and A. Courville, Improved training of Wasserstein GANs, preprint, `arXiv:1704.00028`.

[12] K. Hammernik, T. Klatzer, E. Kobler, M. P. Recht, D. K. Sodickson, T. Pock and F. Knoll, Learning a variational network for reconstruction of accelerated MRI data, *Magnetic Resonance in Medicine*, **79** (2018), 3055–3071.

[13] K. H. Jin, M. T. McCann, E. Froustey and M. Unser, Deep convolutional neural network for inverse problems in imaging, *IEEE Trans. Image Process.*, **26** (2017), 4509–4522.

[14] E. Kang, J. Min and J. C. Ye, A deep convolutional neural network using directional wavelets for low-dose x-ray CT reconstruction, *Medical Physics*, **44** (2017), e360–e375.

[15] V. Kolehmainen, M. Vauhkonen, J. P. Kaipio and S. R. Arridge, Recovery of piecewise constant coefficients in optical diffusion tomography, *Optics Express*, **7** (2000), 468–480.

[16] C. Ledig, L. Theis, F. Huszár, J. Caballero, A. Cunningham, A. Acosta, et al., Photo-realistic single image super-resolution using a generative adversarial network, *IEEE Conference on Computer Vision and Pattern Recognition (CVPR)*, (2017), 105–114.

[17] P.-L. Lions and B. Mercier, Splitting algorithms for the sum of two nonlinear operators, *SIAM J. Numer. Anal.*, **16** (1979), 964–979.

[18] J. Liu, Y. Hu, J. Yang, Y. Chen, H. Shu, L. Luo, et al., 3d feature constrained reconstruction for low-dose CT imaging, *IEEE Transactions on Circuits and Systems for Video Technology*, **28** (2018), 1232–1247.

[19] J. Liu, A. I. Aviles-Rivero, H. Ji and C.-B. Schönlieb, Rethinking medical image reconstruction via shape prior, going deeper and faster: Deep joint indirect registration and reconstruction, preprint, `arXiv:1912.07648`.

[20] J. Liu, H. Ding, S. Molloi, X. Zhang and H. Gao, TICMR: Total image constrained material reconstruction via nonlocal total variation regularization for spectral CT, *IEEE Transactions on Medical Imaging*, **35** (2016), 2578–2586.

[21] J. Liu, T. Kuang and X. Zhang, Image reconstruction by splitting deep learning regularization from iterative inversion, in *Medical Image Computing and Computer Assisted Intervention*, 11070, Lecture Notes in Computer Science, Springer, Cham, 2018, 224–231.

[22] T. Liu, M. Gong and D. Tao, Large-cone nonnegative matrix factorization, *IEEE Trans. Neural Netw. Learn. Syst.*, **28** (2017), 2129–2142.

[23] T. Meinhardt, M. Moller, C. Hazirbas and D. Cremers, Learning proximal operators: Using denoising networks for regularizing inverse imaging problems, in *IEEE International Conference on Computer Vision (ICCV)*, 2017, 1781–1790.

[24] W. Mo and N. Chen, Design of an advanced time-domain diffuse optical tomography system, *IEEE Journal of Selected Topics in Quantum Electronics*, **16** (2010), 581–587.

[25] S. Nowozin, B. Cseke and R. Tomioka, f-GAN: Training generative neural samplers using variational divergence minimization, in *Advances in Neural Information Processing Systems*, 2016, 271–279.

[26] O. Ronneberger, P. Fischer and T. Brox, U-net: Convolutional networks for biomedical image segmentation, in *International Conference on Medical Image Computing and Computer-Assisted Intervention*, 9351, Lecture Notes in Computer Science, Springer, Cham, 2015, 234–241.

[27] L. I. Rudin, S. Osher and E. Fatemi, Nonlinear total variation based noise removal algorithms, *Phys. D*, **60** (1992), 259–268.

[28] J. Sun, H. Li, Z. Xu and Y. Yang, Deep ADMM-Net for compressive sensing MRI, in *Advances in Neural Information Processing Systems*, 2016, 10–18.

[29] A. N. Tihonov, Solution of incorrectly formulated problems and the regularization method, *Soviet Math. Dokl.*, **4** (1963), 1035–1038.

[30] P. Vincent, H. Larochelle, Y. Bengio and P.-A. Manzagol, Extracting and composing robust features with denoising autoencoders, in *Proceedings of the 25th International Conference on Machine learning*, ACM, 2008, 1096–1103.

[31] J. Xie, L. Xu and E. Chen, Image denoising and inpainting with deep neural networks, in *Advances in Neural Information Processing Systems*, 2012, 341–349.

[32] X. Yang, R. Kwitt, M. Styner and M. Niethammer, Quicksilver: Fast predictive image registration– A deep learning approach, *NeuroImage*, **158** (2017), 378–396.

[33] J. Yoo, S. Sabir, D. Heo, K. H. Kim, A. Wahab, Y. Choi, et al., Deep learning diffuse optical tomography, *IEEE Transactions on Medical Imaging*, **39** (2020), 877–887.

E-mail address: matliuj@nus.edu.sg
E-mail address: matjh@nus.edu.sg
E-mail address: biecng@nus.edu.sg